Local Loop Shaping for Rejecting Band-Limited Disturbances in Nonminimum-Phase Systems With Application to Laser Beam Steering for Additive Manufacturing

Tianyu Jiang, Hui Xiao, Jiong Tang, Liting Sun, and Xu Chen

***Abstract*— Closed-loop disturbance rejection without sacrificing overall system performance is a fundamental issue in a wide range of applications from precision motion control, active noise cancellation, to advanced manufacturing. The core of rejecting band-limited disturbances is the shaping of feedback loops to actively and flexibly respond to different disturbance spectra. However, such strong and flexible local loop shaping (LLS) has remained underdeveloped for systems with nonminimum-phase zeros due to challenges to invert the system dynamics. This article proposes an LLS with prescribed performance requirements in systems with nonminimum-phase zeros. Pioneering an integration of the interpolation theory with a model-based parameterization of the closed loop, the proposed solution provides a filter design to match the inverse plant dynamics locally and, as a result, creates a highly effective framework for controlling both narrowband and wideband vibrations. From there, we discuss methods to control the fundamental waterbed limitation, verify the algorithm on a laser beam steering platform in selective laser sintering additive manufacturing, and compare the benefits and tradeoffs over the conventional direct inverse-based loop-shaping method. The results are supported by both simulation and experimentation.**

***Index Terms*— Additive manufacturing, disturbance observer (DOB), disturbance rejection, inverse-free control, local loop shaping (LLS), selective laser sintering (SLS).**

I. Introduction

ACTIVE and flexible shaping of dynamic system responses is central for ubiquitous modern precision systems. For example, modern hard disk drives (HDDs) leverage adaptive disturbance attenuation to achieve nm-scale precision control of the read/write heads [1]–[3]; in smart headphones, active noise cancellation reduces acoustic disturbance transmission from the environment to human ears [4]; and in selective laser sintering (SLS) additive manufacturing, minimizing position errors of galvo mirrors is a key to improve achievable part geometry [5]. In these applications, a certain form of output profile is desired given various band-limited disturbances such as mechanical and acoustic vibrations, yielding the problem of local loop shaping (LLS).

Based on the target disturbance profiles, LLS can be classified as either narrowband or wideband. In the first category, the disturbance spectra concentrate at one or several frequencies. To reject such narrowband disturbances, peak filters [3], [6], [7], repetitive control [8], [9], narrowband Youla parameterization [10]–[12], $\mathcal{H}_\infty$ gain scheduling [13], and narrowband disturbance observer (DOB) [1], [14], [15] can generate corresponding deep, narrow notches in the closed-loop error-rejection functions. For wideband loop shaping, the disturbance energy spans over wide frequency bands. A narrow notch in the error-rejection function can no longer provide sufficient attenuation; yet a wide notch tends to cause undesired amplification at other frequencies due to the fundamental waterbed limitation of feedback control [16]–[18]. In view of such challenges, the authors proposed an infinite-impulse-response (IIR) filter design in DOB to control the waterbed effect manually [15], [19] and optimally [20]; such a design also benefits narrowband disturbance rejection and underpins first-tier results [21], [22] in an international benchmark on adaptive regulation [12]. Reference [23] provides additional comparison of the DOB framework with peak filter algorithms.

Despite current research achievements, strong and flexible LLS has remained challenging for systems with unstable zeros, particularly in applications involving wideband disturbances. Consider controlling a single-input-single-output (SISO) linear time-invariant (LTI) plant P with controller C in a negative feedback loop. Careful stability guarantees must be enforced for algorithms that directly update C [3], [6], [8], [9], [13]. By using a control architecture that

Manuscript received November 1, 2018; revised June 22, 2019; accepted July 12, 2019. Manuscript received in final form August 8, 2019. This work was supported in part by the National Science Foundation under Grant 1750027 and in part by the GE Innovation Fellowship. Recommended by Associate Editor T. Oomen. *(Corresponding author: Xu Chen.)*

T. Jiang, H. Xiao, and X. Chen are with the Department of Mechanical Engineering, University of Washington, Seattle, WA 98195 USA (e-mail: tjiang19@uw.edu; huix27@uw.edu; chx@uw.edu).

J. Tang is with the Department of Mechanical Engineering, University of Connecticut, Storrs, CT 06269 USA (e-mail: jtang@engr.uconn.edu).

L. Sun is with the Department of Mechanical Engineering, University of California at Berkeley, Berkeley, CA 94720 USA (e-mail: litingsun@berkeley.edu).

Color versions of one or more of the figures in this article are available online at http://ieeexplore.ieee.org.

Digital Object Identifier 10.1109/TCST.2019.2934941

intrinsically guarantees stability, algorithms built on Youla parameterization [10], [19], [24]–[26] have the benefit of directly shaping the closed-loop sensitivity function S with, e.g., $S = (1 - NQ/Y)/(1 + PC)$, where transfer functions N and Y come from coprime factorizations of P and C, and transfer function Q is the affine design parameter. For plants with a stable inverse, we have shown that N and Y are reducible to yield the minimum-order factorization $S = (1 - z^{-m}Q)/(1 + PC)$. This is the approach proposed in the aforementioned DOB [1], [19], [21], but has been infeasible for plants with nonminimum-phase zeros. Multiple strategies exist to create stable and realizable model inversions. For example, nonminimum-phase zeros-ignore [27], zero-phase-error-tracking control [28], and zero-magnitude-error-tracking control [29] find transfer function expression of the inversion by replacing the unstable zeros with stable substitutions; iterative learning control (ILC)-based methods construct inverse models by generating impulse responses from feedforward signals [30]; time-domain strategies [31]–[34] aim at identifying the optimal control signal that minimizes the error between a given reference and the output. These inversions apply well to feedforward applications, yet possess only limited functionality and causality for feedback loops.

With the importance of disturbance attenuation on the one hand and the discussed challenges of control design on the other, we propose a new LLS algorithm for shaping the closed-loop response. Compared with previous algorithms such as the DOB, this *forward model selective disturbance observer* (FMSDOB) avoids an explicit plant model inversion and thereby offers freedom and flexibility of loop shaping for nonminimum-phase systems. Compared with other loop-shaping designs, the proposed algorithm inherits the benefits of a DOB regarding design intuition and strong performance [12], [15]. We achieve these benefits by pioneering an integration of the interpolation theory with Youla parameterization and internal model controls to design a class of Q-filters that safely invert the nonminimum-phase plant locally with prescribed feedback functionality. The result is that we can create strong notches flexibly in the closed-loop sensitivity function to reject both narrowband and wideband disturbances. From there, to mitigate undesired amplification from the waterbed effect, we propose techniques to control the frequency response of the Q-filter based on the disturbance spectrum, the performance goals, and the robustness of the overall closed loop. Augmenting these theoretical results, we apply the proposed algorithms in both simulation and experimentation to improve beam scanning in SLS additive manufacturing—a domain where feedback control has been a long-felt but extremely underdeveloped feature for assuring manufacturing quality. During the validation, we further found that for *minimum-phase plants*, the proposed algorithm performs equally well with and even surpasses classical inverse-based DOBs.

The remainder of this article is organized as follows. Section II describes the principle of SLS and the galvo scanner hardware to verify the proposed algorithm. Section III describes the proposed FMSDOB and illustrates the loop shaping philosophy. Section IV develops the main results on filter design for both narrowband and wideband loop shaping. Section V discusses techniques to control the waterbed effect, following which Section VI analyzes the stability and robustness of the proposed method. Section VII summarizes the benefits of the algorithm and the associated tradeoffs. Section VIII provides the simulation and experimental results. Section IX concludes this article.

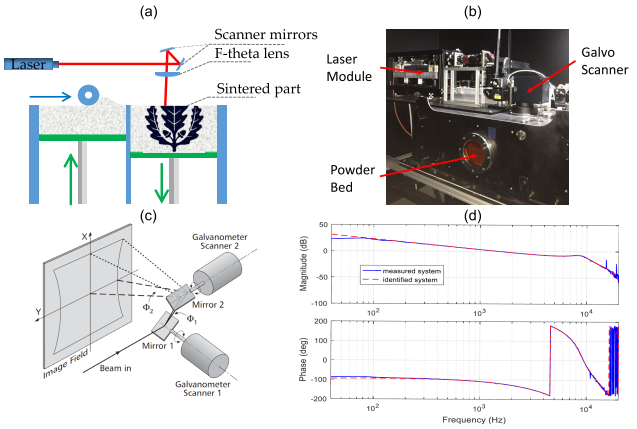

Fig. 1. SLS. (a) Schematic of SLS. (b) In-house built SLS testbed. (c) Galvonometer scanner diagram [36]. (d) Frequency response for one axis of the galvo scanner.

II. Platform Description and Notations

To demonstrate the developed algorithm, we performed simulation and experimentation on a dual-axis galvanometer scanner in SLS, a popular powder-based additive manufacturing process for making high-performance polymeric and metallic parts directly from a digital model [35]. A schematic of SLS is shown in Fig. 1(a). The principle procedures are as follows.

1) Spread a layer of powder, usually 20 μm$\sim$0.1 mm, over the build bed.
2) A galvo scanner controls a laser beam to scan across the powder layer to form a cross-sectional slice of the part.
3) After consolidation, the build surface is lowered by the thickness of a layer, and a new layer is spread by a roller or a blade.
4) The process repeats until the entire 3-D part is created.

Fig. 1(b) shows a picture of an in-house built SLS testbed. As a central element for laser-beam positioning in SLS, the galvo scanner [see Fig. 1(c)] consists of two mini actuation motors with a laser-reflection mirror mounted on each shaft. The incoming laser beam is reflected by the high-reflectance mirrors, the motion of which defines the position of the beam spot on an X-Y Cartesian plane (i.e., the image field). High-precision motion is achieved with a position encoder on the motor that enables closed-loop servos to control the two scanner motors collaboratively. Due to the long distance between the mirrors and image field, small errors in the angular positions Φ_1 and Φ_2 of the mirrors can induce large linear position errors of the beam spot on the powder bed, making the galvo scanner a vibration-sensitive system.

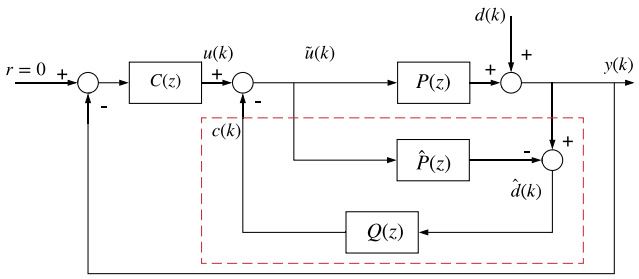

Fig. 2. Proposed FMSDOB scheme.

Fig. 1(d) shows the frequency response for one axis of the galvo, from the voltage input of the motor driver to the voltage output of the encoder that characterizes the motor's position. The system has a bandwidth of around 1000 Hz (with a sampling time of 2.5×10^{-5} s). A picture of the physical system is provided in [5].

Throughout this article, we use the following notation system. $P(z)$ and $P(e^{j\omega})$ denote, respectively, a discrete-time transfer function and its frequency response. $\Re$ and $\Im$ denote, respectively, the real and the imaginary parts of a complex number. The calligraphic $\mathcal{S}$ denotes the set of *stable proper rational transfer functions* and $\mathcal{R}$ denotes the set of *proper rational transfer functions*. $S(\triangleq 1/(1+PC))$ denotes the sensitivity function (i.e., the transfer function from the output disturbance to the plant output) of a feedback loop consisting of a plant P stabilized by an LTI controller C. $T(\triangleq PC/(1+PC))$ denotes the complementary sensitivity function.

III. Forward Model Selective Disturbance Observer

Fig. 2 shows the proposed control scheme. We have the following relevant signals and transfer functions.

1) *P(z) and $\hat{P}$(z):* The plant and its identified model.
2) *C(z):* A baseline controller designed to provide a robustly stable closed loop.
3) *d(k) and $\hat{d}$(k):* The actual (unmeasurable) vibration disturbance and its online estimate.
4) *$\tilde{u}$(k) and u(k):* The control command with and without the compensation signal.
5) *y(k):* Measured residual error.
6) *c(k):* The compensation signal that asymptotically rejects the disturbance *d(k)*.

Assumption 1: Focusing first on nonminimum-phase zeros, we assume that the transfer function $P(z)$ is rational, proper, and stable, but has unstable zeros. We will provide generalizations to unstable plants after introducing the main design principles of the Q-filter.

Assumption 2: The magnitude of $P(e^{j\omega})$ is nonzero at the target disturbance frequencies (otherwise, the disturbance is directly blocked by the plant).

The basic structure of the closed loop employs the underlying principle of internal model control and is a special version of Youla–Kucera parameterization [37]–[40]. To be more specific, general Youla–Kucera parameterization for SISO systems provides Theorem 3.

Theorem 3 ([41], [42]): If a plant $P(=N/D) \in \mathcal{R}$ can be stabilized by a negative-feedback controller $C(=X/Y) \in \mathcal{R}$, with (N, D) and (X, Y) being coprime factorizations over $\mathcal{S}$, then any stabilizing feedback controller of P can be parameterized as

$$C_{all} = \frac{X + DQ}{Y - NQ} : Q \in \mathcal{S}, \quad Y(\infty) - N(\infty)Q(\infty) \neq 0.$$

For the particular problem at hand, letting $X(z) = C(z)$, $Y(z) = 1$, $N(z) = P(z)$, and $D(z) = 1$ (this is feasible under Assumption 1) yields the stabilizing controller

$$C_{all}(z) = \frac{C(z) + Q(z)}{1 - P(z)Q(z)} \tag{1}$$

and Fig. 2 presents one specific realization of the parameterization when $\hat{P}(z) = P(z)$.

Block-diagram analysis gives that if $\hat{P}(z) = P(z)$, then $\hat{d}(k) = d(k)$ in Fig. 2. If $Q(z)$ additionally inverts $P(z)$ at frequencies where $d(k)$ contain major spectral components, then passing $\hat{d}(k)$ through $Q(z)$ (dashed box in Fig. 2) and then through $P(z)$ via the internal negative feedback yields disturbance attenuation.

From a loop shaping perspective, one can obtain the augmented plant dynamics

$$y(k) = P(z)u(k) + (1 - P(z)Q(z))d(k). \tag{2}$$

When $r = 0$, by using $u(k) = -C(z)y(k)$ in (2), the closed-loop dynamics between $d(k)$ and $y(k)$, i.e., the sensitivity function, becomes

$$S(z) = \frac{1 - P(z)Q(z)}{1 + P(z)C(z)} \triangleq S_0(z)(1 - P(z)Q(z)) \tag{3}$$

where $S_0(z) = 1/(1 + P(z)C(z))$ is the original system sensitivity function without the added loop in the dashed box in Fig. 2. Here, if the add-on module $1 - P(z)Q(z) = 0$, then the disturbance transmission is cut off entirely. Of course, in the focused problem setup, $1 - P(z)Q(z) = 0$ over the full frequency range is not achievable because it implies $Q(z) = P^{-1}(z)$, i.e., an unstable inverse. In Section IV, we will design Q to selectively invert the plant dynamics for controlling general band-limited disturbances. Then, we will circle back to discuss the case when the plant contains uncertainties [i.e., $P(z) \neq \hat{P}(z)$].

IV. Main Results

A. Pointwise Selective Model Inversion

We consider first a pointwise inverse of P such that

$$Q(e^{j\omega_i})P(e^{j\omega_i}) = 1 \tag{4}$$

at a set of target frequencies $\{\omega_i : \omega_i \in (0, \pi), i = 1, 2, \ldots, n\}$ ($\omega_i \neq \omega_j$, $\forall i \neq j$).

Under Assumption 2, the equation translates to

$$Q(e^{j\omega_i}) = \frac{1}{P(e^{j\omega_i})} = \frac{\overline{P(e^{j\omega_i})}}{|P(e^{j\omega_i})|^2}$$

that is

$$\begin{cases} \Im Q(e^{j\omega_i}) = -\dfrac{\Im P(e^{j\omega_i})}{|P(e^{j\omega_i})|^2} \\ \Re Q(e^{j\omega_i}) = \dfrac{\Re P(e^{j\omega_i})}{|P(e^{j\omega_i})|^2}, \end{cases} \quad i = 1, 2, \ldots, n. \tag{5}$$

Proposition 4: Let

$$Q(z) = q_0 + \sum_{l=1}^{m} q_l z^{-l} \tag{6}$$

with

$$\begin{bmatrix} q_0 \\ \vdots \\ q_m \end{bmatrix} = \begin{bmatrix} 1 & \cos\omega_1 & \ldots & \cos m\omega_1 \\ 0 & \sin\omega_1 & \ldots & \sin m\omega_1 \\ \vdots & & & \vdots \\ \vdots & & & \vdots \\ 1 & \cos\omega_n & \ldots & \cos m\omega_n \\ 0 & \sin\omega_n & \ldots & \sin m\omega_n \end{bmatrix}^{-1} \begin{bmatrix} \dfrac{\Re P(e^{j\omega_1})}{|P(e^{j\omega_1})|^2} \\ \dfrac{\Im P(e^{j\omega_1})}{|P(e^{j\omega_1})|^2} \\ \vdots \\ \vdots \\ \dfrac{\Re P(e^{j\omega_n})}{|P(e^{j\omega_n})|^2} \\ \dfrac{\Im P(e^{j\omega_n})}{|P(e^{j\omega_n})|^2} \end{bmatrix} \tag{7}$$

where $m = 2n - 1$. Then

$$Q(e^{j\omega_i})P(e^{j\omega_i}) = 1 \quad \forall i = 1, 2, \ldots, n.$$

Proof: Let $Q(e^{j\omega}) = q_0 + \sum_{l=1}^{m} q_l e^{-jl\omega}$, where $m(\in \mathbb{Z})$ is the order of the filter. Based on (5), we must have, for $i = 1, 2, \ldots, n$

$$q_0 + \sum_{l=1}^{m} q_l \cos l\omega_i = \frac{\Re P(e^{j\omega_i})}{|P(e^{j\omega_i})|^2}$$
$$\sum_{l=1}^{m} q_l \sin l\omega_i = \frac{\Im P(e^{j\omega_i})}{|P(e^{j\omega_i})|^2}.$$

In the matrix form, the above is equivalent to

$$\begin{bmatrix} 1 & \cos\omega_i & \ldots & \cos m\omega_i \\ 0 & \sin\omega_i & \ldots & \sin m\omega_i \end{bmatrix} \begin{bmatrix} q_0 \\ \vdots \\ q_m \end{bmatrix} = \begin{bmatrix} \dfrac{\Re P(e^{j\omega_i})}{|P(e^{j\omega_i})|^2} \\ \dfrac{\Im P(e^{j\omega_i})}{|P(e^{j\omega_i})|^2} \end{bmatrix}. \tag{8}$$

There are n such equation sets or $2n$ linear equations. When $\omega_i \in (0, \pi)$, the rows of the matrix on the left-hand side are all linearly independent for different values of ω_i. We thus have $2n$ linearly independent equations and $m+1$ unknowns, and the minimum order of $Q(z)$ for the existence of a unique solution is $m + 1 = 2n$. Under this case, the solutions to q_i values are given by (7). ■

Proposition 4 relaxes the requirement of a full stable inverse by focusing on $P^{-1}(e^{j\omega_i})$ at selective regions based on the target disturbance profiles. For implementation, one can selectively measure the frequency response of the plant in regions where loop shaping is desired. Putting these data into the vector on the right-hand side (RHS) of (7), one can obtain the Q solution for target loop shaping. Adaptation is further possible, given a known or online identified $P(e^{j\omega_i})$ (Section VIII).

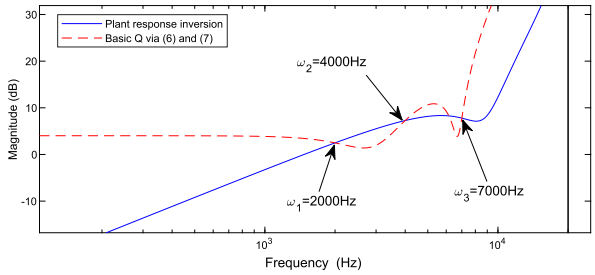

Fig. 3. Comparison of the inverse frequency response of the plant and frequency response of the proposed Q-filter.

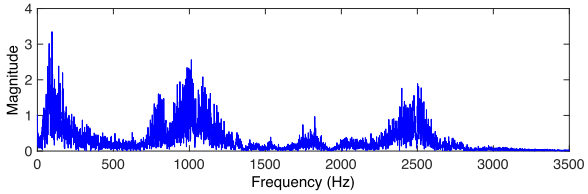

Fig. 4. Example of wideband disturbance spectrum [2].

Example 5: The nominal transfer function for the galvo scanner described in Fig. 1(d) is given by

$$P(z) = \frac{0.0282z^2 + 0.1504z + 0.1146}{z^4 - 1.3190z^3 + 0.929z^2 - 0.6073z - 0.0035} \tag{9}$$

with a sampling time of $T_s = 2.5 \times 10^{-5}$ s. Then, for three narrowband disturbances $\omega_1 = 0.1\pi$, $\omega_2 = 0.2\pi$, and $\omega_3 = 0.35\pi$ (or 2000, 4000, and 7000 Hz), a Q-filter with order $m = 5$ is needed. Solving (7) gives $[\, q_0 \; q_1 \; q_2 \; q_3 \; q_4 \; q_5 \,]^T = [\, 22.6 \; -88.0 \; 149.7 \; -147.1 \; 82.9 \; -21.7 \,]^T$. The comparison result between the frequency responses $P^{-1}(e^{j\omega})$ and $Q(e^{j\omega})$ is shown in Fig. 3. The intersection points at 2000, 4000, and 7000 Hz show that (4) is achieved at the target frequencies.

B. Higher Order Wideband Inversion

Compared with single-frequency excitations, wideband disturbances (see Fig. 4) induce widely spanned spectral peaks. For such disturbances, pointwise inversion of the plant alone will not generate satisfying result. The reason, as can be seen in Fig. 3, is that the slopes of the frequency responses $P^{-1}(e^{j\omega})$ and $Q(e^{j\omega})$ differ from each other at the intersection points. In other words, because $Q(e^{j\omega})$ only interpolates $1/P(e^{j\omega})$ at ω_i, when the frequency deviates from these points, the difference between $1/P(e^{j\omega})$ and $Q(e^{j\omega})$ increases quickly. As a result, the frequency response of $1 - PQ$, both magnitude and phase, can easily fall out of the prescribed performance threshold. To address the limitation, we propose an augmented Q-filter to minimize the frequency response of $1 - PQ$ in each frequency band by controlling both $1 - P(e^{j\omega})Q(e^{j\omega})$ and its derivative. This yields a selective Hermite interpolation [43] of $1/P(e^{j\omega})$ and expands significantly the approximation region.

Proposition 6: Let $\omega_i \in (0, \pi)$, $i = 1, 2, \ldots, n$ be the center frequencies of the wideband disturbance. Let (N, D) be a coprime factorization of $P(z)$ such that $P = ND^{-1}$,

where $N=\sum_{u=0}^{p} b_u z^u$ and $D=z^q+\sum_{v=0}^{q-1} a_v z^v$. Design $Q(z)=q_0+\sum_{l=1}^{m} q_l z^{-l}$ with $m=4n-1$ and

$$\begin{bmatrix} q_0 \\ \vdots \\ q_m \end{bmatrix} = \begin{bmatrix} 1 & \cos\omega_1 & \cos 2\omega_1 & \dots & \cos m\omega_1 \\ 0 & \sin\omega_1 & \sin 2\omega_1 & \dots & \sin m\omega_1 \\ \vdots & & & & \vdots \\ 1 & \cos\omega_n & \cos 2\omega_n & \dots & \cos m\omega_n \\ 0 & \sin\omega_n & \sin 2\omega_n & \dots & \sin m\omega_n \\ 0 & \cos\omega_1 & 2\cos 2\omega_1 & \dots & m\cos m\omega_1 \\ 0 & \sin\omega_1 & 2\sin 2\omega_1 & \dots & m\sin m\omega_1 \\ \vdots & & & & \vdots \\ 0 & \cos\omega_n & 2\cos 2\omega_n & \dots & m\cos m\omega_n \\ 0 & \sin\omega_n & 2\sin 2\omega_n & \dots & m\sin m\omega_n \end{bmatrix}^{-1} \times \begin{bmatrix} \frac{\Re P(e^{j\omega_1})}{|P(e^{j\omega_1})|^2} \\ \frac{\Im P(e^{j\omega_1})}{|P(e^{j\omega_1})|^2} \\ \vdots \\ \frac{\Re P(e^{j\omega_n})}{|P(e^{j\omega_n})|^2} \\ \frac{\Im P(e^{j\omega_n})}{|P(e^{j\omega_n})|^2} \\ -\Re H(e^{j\omega_1}) \\ \Im H(e^{j\omega_1}) \\ \vdots \\ -\Re H(e^{j\omega_n}) \\ \Im H(e^{j\omega_n}) \end{bmatrix} \tag{10}$$

where

$$H(e^{j\omega}) = \frac{\left(qe^{jq\omega}+\sum_{v=1}^{q-1} va_v e^{jv\omega}\right)N(e^{j\omega})-\sum_{u=1}^{p} ub_u e^{ju\omega}D(e^{j\omega})}{N^2(e^{j\omega})}$$

then

$$\begin{cases} 1-P(e^{j\omega_i})Q(e^{j\omega_i}) & =0 \\ \dfrac{\mathrm{d}}{\mathrm{d}\omega}(1-P(e^{j\omega})Q(e^{j\omega}))\Big|_{\omega=\omega_i} & =0. \end{cases} \tag{11}$$

Proof: The first equation in (11) has been proved in Proposition 4 and the resulting properties have been reserved in (10). We only need to assure $(\mathrm{d}/\mathrm{d}\omega)(1-P(e^{j\omega})Q(e^{j\omega}))\,|_{\omega=\omega_i}=0$, that is

$$\begin{aligned} &\frac{\mathrm{d}}{\mathrm{d}\omega}(1-P(e^{j\omega})Q(e^{j\omega}))\Big|_{\omega=\omega_i} \\ &= -\frac{\mathrm{d}}{\mathrm{d}\omega}(P(e^{j\omega})Q(e^{j\omega}))\Big|_{\omega=\omega_i} \\ &= -\left(\frac{\mathrm{d}P(e^{j\omega})}{\mathrm{d}\omega}Q(e^{j\omega})+\frac{\mathrm{d}Q(e^{j\omega})}{\mathrm{d}\omega}P(e^{j\omega})\right)\Big|_{\omega=\omega_i} \\ &= 0. \end{aligned} \tag{12}$$

Note that $1-P(e^{j\omega_i})Q(e^{j\omega_i})=0$. Under Assumption 2 [$P(e^{j\omega_i})\neq 0$], (12) becomes

$$\left(\frac{\mathrm{d}P(e^{j\omega})}{\mathrm{d}\omega}\frac{1}{P(e^{j\omega})}+\frac{\mathrm{d}Q(e^{j\omega})}{\mathrm{d}\omega}P(e^{j\omega})\right)\Big|_{\omega=\omega_i}=0$$

that is

$$\frac{\mathrm{d}Q(e^{j\omega})}{\mathrm{d}\omega}\Big|_{\omega=\omega_i} = -\frac{1}{P^2(e^{j\omega})}\frac{\mathrm{d}P(e^{j\omega})}{\mathrm{d}\omega}\Big|_{\omega=\omega_i} = \frac{\mathrm{d}}{\mathrm{d}\omega}\frac{1}{P(e^{j\omega})}\Big|_{\omega=\omega_i}. \tag{13}$$

Given $Q(z)=q_0+\sum_{l=1}^{m} q_l z^{-l}$, the left-hand side of (13) is

$$\frac{\mathrm{d}Q(e^{j\omega})}{\mathrm{d}\omega}|_{\omega=\omega_i} = -\sum_{l=1}^{m} q_l l\sin l\omega_i - j\sum_{l=1}^{m} q_l l\cos l\omega_i. \tag{14}$$

Given the FIR coprime factorization of $P=ND^{-1}$, the RHS of (13) becomes

$$\begin{aligned} &\frac{\mathrm{d}}{\mathrm{d}\omega}\frac{1}{P(e^{j\omega})}\Big|_{\omega=\omega_i} \\ &= \frac{\mathrm{d}}{\mathrm{d}z}\frac{1}{P(z)}\frac{\mathrm{d}z\,(=e^{j\omega})}{\mathrm{d}\omega}\Big|_{\omega=\omega_i} \\ &= \frac{\mathrm{d}}{\mathrm{d}z}\frac{D(z)}{N(z)}\frac{\mathrm{d}e^{j\omega}}{\mathrm{d}\omega}\Big|_{\omega=\omega_i} \\ &= j\frac{\frac{\mathrm{d}}{\mathrm{d}z}D(z)N(z)-\frac{\mathrm{d}}{\mathrm{d}z}N(z)D(z)}{N^2(z)}z\Big|_{z=e^{j\omega_i}} \\ &= j\frac{(qz^q+\sum_{v=1}^{q-1} va_v z^v)N(z)-(\sum_{u=1}^{p} ub_u z^u)D(z)}{N^2(z)}\Big|_{z=e^{j\omega_i}} \\ &= jH(e^{j\omega_i}). \end{aligned} \tag{15}$$

Matching the real and the imaginary parts of (14) and (15) for $i=1,2,\dots,n$ gives the lower half of (10). There are $4n$ linear independent equations in (10), and the minimum order of Q for the existence of a unique solution is $m=4n-1$. ∎

For implementation, one can either substitute $P(z)$ with $\hat{P}(z)$ in Proposition 6 and calculate $H(e^{j\omega})$ based on the analytic transfer function or directly calculate the derivative of $P^{-1}(e^{j\omega})$ in (13) using a measured frequency response.

Corollary 7: If (11) is true, then

$$\frac{\mathrm{d}}{\mathrm{d}\omega}|1-P(e^{j\omega})Q(e^{j\omega})|\,|_{\omega=\omega_i}=0.$$

Proof: Assume that $1-P(e^{j\omega})Q(e^{j\omega})=A(\omega)e^{j\theta(\omega)}$, where $A(\omega)$ and $\theta(\omega)$ are the magnitude and the phase responses, respectively. Then

$$\frac{\mathrm{d}}{\mathrm{d}\omega}(1-P(e^{j\omega})Q(e^{j\omega}))=\frac{\mathrm{d}A(\omega)}{\mathrm{d}\omega}e^{j\theta(\omega)}+jA(\omega)\frac{\mathrm{d}\theta(\omega)}{\mathrm{d}\omega}e^{j\theta(\omega)}.$$

Note that $A(\omega_i)=0$. The above equation then gives

$$\frac{\mathrm{d}}{\mathrm{d}\omega}(1-P(e^{j\omega})Q(e^{j\omega}))\,|_{\omega=\omega_i}=\frac{\mathrm{d}A(\omega)}{\mathrm{d}\omega}e^{j\theta(\omega)}\,|_{\omega=\omega_i}=0$$

which is equivalent to

$$\frac{\mathrm{d}A(\omega)}{\mathrm{d}\omega}=\frac{\mathrm{d}}{\mathrm{d}\omega}\left|1-P(e^{j\omega})Q(e^{j\omega})\right|\,|_{\omega=\omega_i}=0.$$

∎

Therefore, the Q-filter design in (10) guarantees that the first-order derivative of the magnitude response of $1-PQ$ is zero at the target frequencies.

Consider again Example 5. Fig. 5 shows the frequency response of the proposed wideband $Q(e^{j\omega})$ from (10).

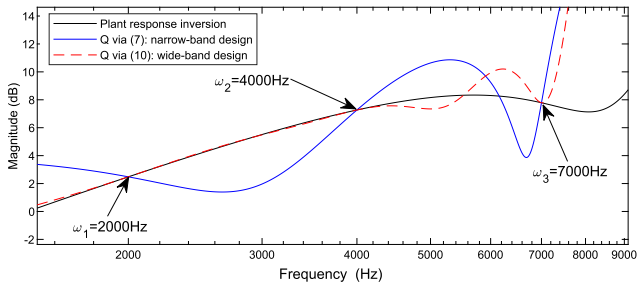

Fig. 5. Comparison of magnitude response of Q for narrowband and wideband designs.

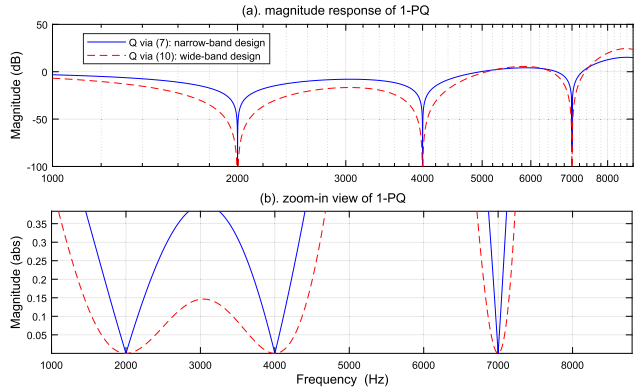

Fig. 6. Comparison of magnitude response of 1-PQ for narrowband and wideband designs. (a) Magnitude response of 1-PQ. (b) Zoomed-in view of 1-PQ.

Compared to the basic solution (7), the magnitude response of the filter matches the inverse magnitude response of $P(z)$ within wide ranges around the target frequencies. Therefore, $|1 - Q(e^{j\omega})P(e^{j\omega})| < \epsilon$ within a wideband for a prescribed performance threshold ϵ. Indeed, in the magnitude response of $1 - PQ$ (Fig. 6), the filter design that incorporates the derivative dynamics gives wider notch shapes at all three disturbance frequencies. A zoomed-in view of the notch shape of $1 - PQ$ in linear scale shows that the proposed design for wideband disturbance indeed achieves zero derivative at the target frequencies and thereby induces wider range disturbance attenuation.

Remark 8 (Extension to Unstable Plants): When P is unstable, instead of the discussed factorization $S = (1 - PQ)/(1+PC)$, general Youla parameterization gives $S = (1-NQ/Y)/(1 + PC)$, with $P = N/D$ and $C = X/Y$. The same design procedure applies to Q, with the replacement of P by N/Y in Proposition 4 and analogous modifications of H in Proposition 6.

C. Band-Selection Filter

Proposition 4 provides an FIR filter design that achieves the desired disturbance rejection at ω_i. However, because there is no constraint on the overall magnitude of Q, this basic solution can induce disturbance amplification when $\omega \neq \omega_i$, especially at frequencies far away from the target frequency. Meanwhile, at frequencies where large model uncertainties and mismatches exist, high-performance control has to be sacrificed intrinsically for robustness based on robust control theory. Thus, we propose to incorporate special bandpass characteristics to maintain the magnitude of $Q(e^{j\omega})$ small when $\omega \neq \omega_i$.

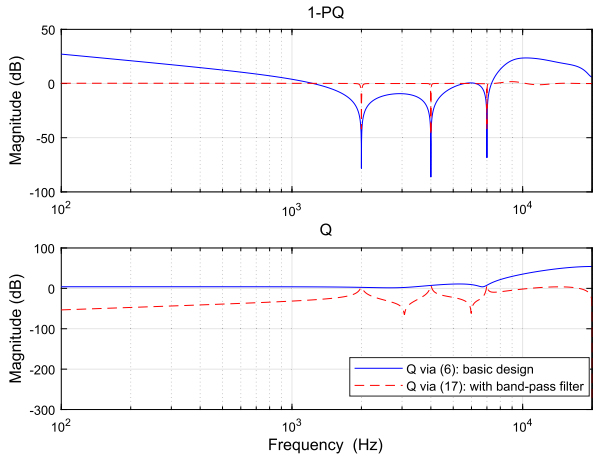

Fig. 7. Comparison of frequency response for the Q-filter with and without bandpass filter.

We propose the following lattice-structure [44] bandpass filter:

$$Q_{BP}(z) = 1 - \frac{1}{2^n}\prod_{i=1}^{n}\frac{(1+k_{2,i})(1+2k_{1,i}z^{-1}+z^{-2})}{1+k_{1,i}(1+k_{2,i})z^{-1}+k_{2,i}z^{-2}} \quad (16)$$

where $k_{1,i} = -\cos\omega_i$ and $k_{2,i} = [1 - \tan(B_{w,i}/2)]/[1 + \tan(B_{w,i}/2)]$, and $B_{w,i}$ (in radian) is the 3-dB bandwidth of $Q_{BP}(z)$ centered around ω_i. It can be shown that $Q_{BP}(e^{j\omega_i}) = 1, (\mathrm{d}/\mathrm{d}\omega)|Q_{BP}(e^{j\omega})||_{\omega=\omega_i} = 0$, $\forall i = 1, 2, \ldots, n$.

Applying (16) to (7) yields the improved design

$$Q(z) = Q_{BP}(z)\left(q_0 + \sum_{l=1}^{2n-1} q_l z^{-l}\right) \quad (17)$$

which not only reserves the disturbance rejection properties but also avoids amplification of noises in $d(k)$ outside the target frequency ranges. Applying the filter with center frequency $\omega = [0.1\pi\ 0.2\pi\ 0.35\pi]$ and the width of passbands $B_{w,i} = 2 \times 10^{-3}\pi$ (or 40 Hz when $T_s = 2.5 \times 10^{-5}$ s) to Example 5, we obtain the frequency responses of $1-PQ$ and Q in Fig. 7. Compared with the basic design via (6), the proposed Q enhancement not only possesses the needed bandpass shape but also greatly mitigates the large magnitude amplification of $1 - PQ$ at frequencies far from the centers of the passbands, especially at low and high frequencies.

V. Control of the Waterbed Effect

In Section IV, we proposed a bandpass filter that controls the undesired disturbance amplification. However, note that no practical bandpass filter is ideal (that is, having zero phase response and a rectangular magnitude response), especially when the passband gets wider. Therefore, it is infeasible for (17) to maintain 0 everywhere outside the target frequency bands. As a result, along with the desired notch shape,

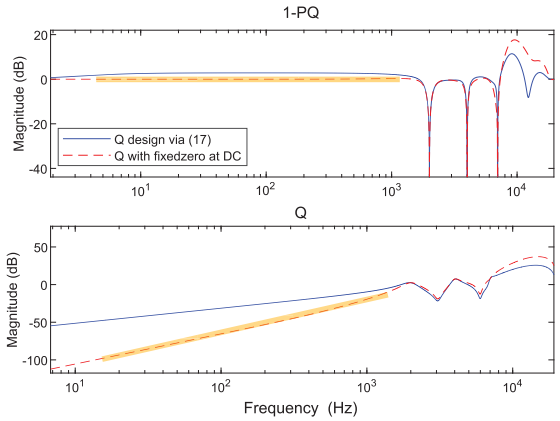

Fig. 8. Effect of a fixed zero at low-frequency region.

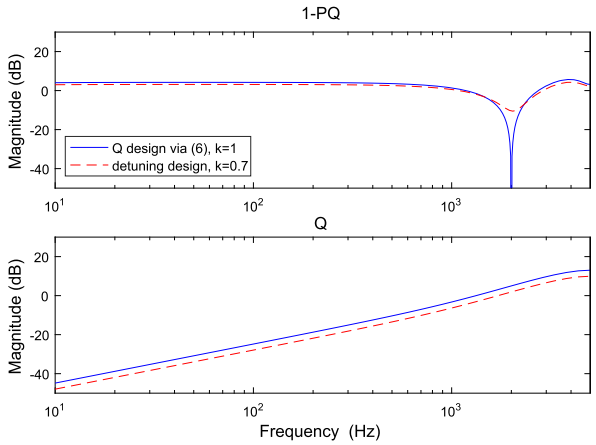

Fig. 9. Effect of detuning for narrowband loop shaping.

the magnitude of $1-P(e^{j\omega})Q(e^{j\omega})$ will exhibit the waterbed effect of exceeding 1. In this section, we discuss the frequency-domain closed-loop properties and how to control the relevant performance limitations.

Corollary 9: Take any P and Q that are stable and causal. The magnitude response of $1-P(e^{j\omega})Q(e^{j\omega})$ satisfies

$$\int_0^{\pi} \ln|1-P(e^{j\omega})Q(e^{j\omega})|\mathrm{d}\omega = \pi\left(\sum_{i=1}^{n_\gamma}\ln|\gamma_i| - \ln|\sigma+1|\right) \tag{18}$$

where $\{\gamma_i\}_{i=1}^{n_\gamma}$ $(n_\gamma \geq 0)$ is the set of unstable zeros of $1-P(z)Q(z)$ ($\{\gamma_i\}_{i=1}^{n_\gamma}$ is the empty set if $n_\gamma = 0$), and

$$\sigma = \lim_{z\to\infty} P(z)Q(z)/(1-P(z)Q(z)).$$

Proof: The proof is analogous to the one in [45] and omitted here. ∎

For plants whose relative degree is zero, we have $\lim_{z\to\infty} P(z) \neq 0$. It is then possible that $\sigma > 0$ and the integral on the RHS of (18) is less than zero. However, for strictly proper plants (the more common case), $\lim_{z\to\infty} P(z) = 0$ and $\sigma = 0$; (18) simplifies to $\int_0^{\pi} \ln|1-P(e^{j\omega})Q(e^{j\omega})|d\omega = \pi\sum_{i=1}^{n_\gamma}\ln|\gamma_i| \geq 0$. Then, it is inevitable that there exist frequencies where $|1-P(e^{j\omega})Q(e^{j\omega})| > 1$. In other words, some disturbance energies (noises) are amplified in (2).

Although the overall area integral is constrained in (18), by proper structural design in $Q(z)$, the waterbed effect can be controlled based on the disturbance spectra, the performance goals, and the availability of accurate plant information in different regions. This is the primary reason for the bandpass design in (17). Further enhancement can be made, as we will now discuss in the following paragraphs.

The first method for enhanced waterbed control is to add fixed zeros to $Q(z)$ to constrain the magnitude of $1-P(e^{j\omega})Q(e^{j\omega})$. Fig. 8 shows the effect of placing a zero in $Q(z)$ near $z = 1$ (dc gain). Recall the sensitivity function in (3). The induced small gain of $Q(e^{j\omega})$ at low frequency successfully reduces $|1-P(e^{j\omega})Q(e^{j\omega})|$ in the highlighted region in Fig. 8 and, hence, reduces the magnitude response of the sensitivity function in (3). On the other hand, if the noise frequency is high, introducing a fixed zero near $z = -1$ provides enhanced small gain for $Q(e^{j\omega})$ at high frequencies. Furthermore, combined fixed zeros near the noise frequency can enhance the bandpass property. This method of zero modulation is especially effective when knowledge of noise spectrum in $d(k)$ is available.

From the algorithmic viewpoint, a pair of fixed zeros $\rho e^{\pm j\omega_p}$, $\omega_p \in (0,\pi)$ translate to

$$Q(\rho e^{j\omega_p}) = q_0 + \sum_{l=1}^{m} q_l(\rho e^{j\omega_p})^{-l} = 0$$

namely

$$\Re Q(\rho e^{j\omega_p}) = q_0 + \sum_{l=1}^{m} q_l \frac{1}{\rho^l}\cos l\omega_p = 0$$

$$\Im Q(\rho e^{j\omega_p}) = -\sum_{l=1}^{m} q_l \frac{1}{\rho^l}\sin l\omega_p = 0.$$

Two additional equations thus need to be added to (7)

$$\begin{bmatrix} 1 & \frac{1}{\rho}\cos\omega_p & \dots & \frac{1}{\rho^m}\cos m\omega_p \\ 0 & \frac{1}{\rho}\sin\omega_p & \dots & \frac{1}{\rho^m}\sin m\omega_p \end{bmatrix} \begin{bmatrix} q_0 \\ \vdots \\ q_m \end{bmatrix} = \begin{bmatrix} 0 \\ 0 \end{bmatrix} \tag{19}$$

and the minimum order of $Q(z)$ becomes $m = 2n+1$ if $\omega_p \neq 0$ and $\omega_p \neq \pi$. When $\omega_p = 0$ or π, the second equation in (19) can be removed and the minimum order reduces to $m = 2n$. For the case with n_{p_0} added zeros at 0, n_{p_π} added zeros at π, and n_p added zeros elsewhere, the condition for a minimum-order solution of $Q(z)$ is $m+1 = 2n+2n_p+n_{p_0}+n_{p_\pi}$, i.e., $m = 2n+2n_p+n_{p_0}+n_{p_\pi}-1$.

Another direct approach to reducing the overall waterbed amplification is to first design a regular Q-filter in (6) and then detune the magnitude response by letting $\tilde{Q}(z) = kQ(z)$, $k \in (0,1)$. Fig. 9 presents the effect of applying such a design with $k = 0.7$. The smaller gain at both low- and high-frequency regions shows that the amplification is indeed mitigated. The proposed detuning relaxes the waterbed effect because unstable zeros of $1-P(z)Q(z)$, if any, can be pulled into the unit circle by cascading the gain k. In fact,

as $k \to 0$, the zeros of $1 - kP(z)Q(z)$ approximate the poles of $P(z)Q(z)$, which are all stable.

VI. Stability and Robustness

This section analyzes the closed-loop stability and robust stability of the proposed control scheme. For stability, we have the following result from closed-loop characteristic equation:

Proposition 10: If $P(z)$ and $Q(z)$ are stable and $\hat{P}(z) = P(z)$, then the closed-loop system in Fig. 2 is stable.

Proof: In Fig. 2, we have the relationships

$$\begin{cases} U(z) = -C(z)Y(z) \\ C(z) = [((U(z) - C(z))(P(z) - \hat{P}(z))]Q(z) \\ Y(z) = P(z)((U(z) - C(z)) + D(z). \end{cases}$$

Eliminating $U(z)$ and $C(z)$ gives the closed-loop transfer function

$$Y(z) = \frac{1 - P(z)Q(z) + Q(z)(P(z) - \hat{P}(z))}{1 + P(z)C(z) + Q(z)(P(z) - \hat{P}(z))} D(z).$$

Let $P(z) = B_P(z)/A_P(z)$, $\hat{P}(z) = B_{\hat{P}}(z)/A_{\hat{P}}(z)$, $C(z) = B_C(z)/A_C(z)$, and $Q(z) = B_Q(z)/A_Q(z)$ be the coprime polynomial factorization of $P(z)$, $\hat{P}(z)$, $C(z)$, and $Q(z)$. When $\hat{P}(z) = P(z)$, the closed-loop characteristic equation becomes

$$A_Q(z)A_{\hat{P}}(z)[A_P(z)A_C(z) + B_P(z)B_C(z)] = 0.$$

Hence, the closed-loop poles are composed of the baseline closed-loop poles and the poles of $Q(z)$ and $\hat{P}(z)$. As the baseline feedback loop, $Q(z)$, and $\hat{P}(z)$ [$=P(z)$] are all stable, the new closed loop is thus stable. ■

For *robust stability*, when the plant is perturbed to be $\tilde{P}(z) = P(z)(1 + \Delta(z)) = \hat{P}(z)(1 + \Delta(z))$ [the uncertainty $\Delta(z)$ is assumed to be stable and has a bounded $\mathcal{H}_\infty$ norm], applying the small-gain theorem yields the following robust-stability condition:

$$\|\Delta(z)T(z)\|_\infty < 1 \tag{20}$$

where T is the nominal complementary sensitivity function satisfying $T = 1 - S$. After substituting in (3), (20) becomes

$$\left\| \Delta(z)P(z)\frac{C(z) + Q(z)}{1 + P(z)C(z)} \right\|_\infty < 1.$$

Equation (20) implies that in order to preserve the robust stability, magnitude of the plant uncertainty has to be lower than that of $1/T(z)$. Fig. 10 shows the magnitude response of $1/T(z)$ when rejecting disturbance at 4000 Hz for the plant in (9) with different Q designs. Fig. 10 (top) indicates that compared to the baseline open-loop system, introducing the proposed FMSDOB largely preserves the robust stability bounds. The minimal value of $|\ 1/T(z)\ |$ for both the narrowband and wideband designs is -0.15 dB at around 4097 Hz, i.e., the plant uncertainty can be as large as 98.3% at all frequencies without causing instability. The necessity of the bandpass filter in (16) is evident from Fig. 10 (bottom). Without the filter, the minimal value of $|\ 1/T(z)\ |$ decreases

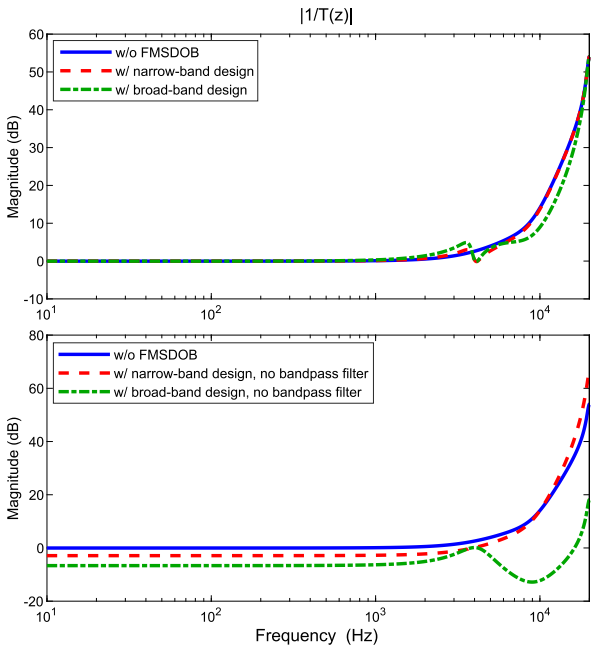

Fig. 10. Magnitude response of $1/T(z)$ defines the upper bounds for plant uncertainty to preserve robust stability.

to -2.9 dB (71.6%) at the low-frequency region for narrow-band design and -12.82 dB (22.9%) at around 9001 Hz for wideband design.

When rejecting multiple, especially wideband high-frequency disturbances, the requirement on the magnitude of uncertainty can be stringent to assure the stability. Such a tradeoff between performance and robustness is more significant for nonminimum-phase systems [recall (18)]. Engineering practice can balance the tradeoff by leveraging the proposed bandpass filter, detuning factor, and sometimes a low-pass filter that turns off the compensation at high-frequency region. In Section VIII, we provide an example implementation of the algorithm subject to model mismatch and show that high performance can still be maintained with the design flexibility of the algorithms.

VII. Summary and Application Recommendations

We have proposed a disturbance rejection scheme that can be used in systems with nonminimum-phase zero(s). Under this framework, two Q-filter designs based on local plant dynamics have been introduced. In general, when the disturbance energy concentrates at one or several individual frequencies, the narrowband design in (7) is sufficient to reject the disturbance without introducing severe deterioration at other frequencies. The wideband design as described in (10) is ideal when the disturbance energy spans over wide frequency bands.

The proposed scheme suits particularly for disturbance rejection that desires the following algorithmic properties.

1) *No Direct Plant Inversion:* The proposed design eliminates the parasitic complexity associated with a direct plant inversion in feedback applications.
2) *Flexibility and Accuracy:* Compared with existing plant inversion algorithms for a nonminimum-phase system,

the proposed method offers new flexibility and accuracy to feedback controls. The proposed pointwise inverse allows for full disturbance rejection at selective regions. The design of Q requires only selective frequency responses [RHS of (7) and (10)] instead of an inverse transfer-function plant model, which may be difficult or even infeasible in practice.

3) *Design Intuition, Performance, and Extensions:* A regular inverse-based DOB structure with low-pass Q design focuses more on the magnitude and does not explicitly consider the phase compensation that can significantly deteriorate the achievable performance at high frequencies. In contrast, both the magnitude and phase compensations are taken into consideration in (4). Compared with other loop-shaping algorithms, the proposed scheme inherits the advantages of flexible intuitive design and high performance of the DOB [12], [21]. It also shares the capability of easy adaptation [21], [23] (see Section VIII-A).

Certainly, any control design is subject to tradeoffs in practice. The fundamental limits of feedback control and plant uncertainties should still be respected. In practice, we recommend to test the basic solutions in Section IV first, and when the "waterbed"-induced amplifications are severe in the basic solutions, one can use such enhancement techniques as bandpass filters, fixed zeros, and tuning factors based on the disturbance spectra. We recommend to start with a baseline feedback loop (e.g., by forming a PID or H_∞ controller C in Fig. 2), then to iterate the LLS design until a satisfying frequency response of $1 - PQ$ is obtained.

VIII. Simulation and Experimentation

In this section, we verify the proposed scheme for both narrowband and wideband loop shaping in the laser beam steering for SLS. Along the way, we compare the efficiency of the algorithm with the conventional inverse-based DOB.

A. Narrowband Loop Shaping and Performance Comparison

In Fig. 2, let one axis of the laser galvo scanner described in Section II be $P(z)$. For a fair comparison with conventional inverse design algorithms, we sample the system at a sampling time of $T_s = 1\times10^{-4}$ s, yielding the following nominal model with stable zeros:

$$\hat{P}(z) = \frac{0.5465z^3 + 0.4598z^2 - 0.0717z - 0.0721}{z^4 - 0.5221z^3 - 0.6208z^2 + 0.0730z + 0.0721}.$$

We set $C(z) = 1$ because a vendor-integrated baseline controller is already embedded in $P(z)$.

A series of time-varying narrowband vibrations is considered in both simulation and experiment. The disturbance frequency varies in the pattern of null $\rightarrow$ 500 Hz $\rightarrow$ 1500 Hz $\rightarrow$ 500 Hz $\rightarrow$ 3000 Hz $\rightarrow$ 500 Hz $\rightarrow$ null with step frequency changes between each disturbance section. The first disturbance is injected at 0.5 s and the duration time for each frequency is 0.3 s. The amplitude of the disturbance is 0.1 V. The inherent disturbance estimation and LLS design in the proposed algorithm enable easy adaptation of the controller parameters. Fig. 11 presents the online identified frequencies using a parameter adaptation algorithm (PAA) detailed in [21]. Fig. 12 (top) shows the simulated time trace of the residual position errors. The proposed algorithm using a $Q(z)$ filter in (17), with the bandwidth of the lattice bandpass filter set as 50 Hz, is seen to provide rapid and strong vibration attenuation. Inspection of data at 0.79, 1.09, and 1.69 s indicates that the steady-state position errors indeed converge to zero. The experimental results of rejecting the same disturbance are shown in Fig. 12 (bottom). There, the compensation scheme reduces steady-state errors to the same as or even smaller than the baseline case. This is also verified by calculating the 2-norm of the steady-state errors (denoted as $\|e_r\|_2^2$) in the time windows indicated by the dashed frames in Fig. 12 (bottom). The corresponding results are given in Table I. The physical system has nonstationary noises from the electric circuits and the operation environments, as well as small nonlinearities in position sensing (e.g., in the magnitude of mrad optical/44°), hence the minor statistical variations in the numbers in Table I. Yet the controller has maintained its effectiveness in all time

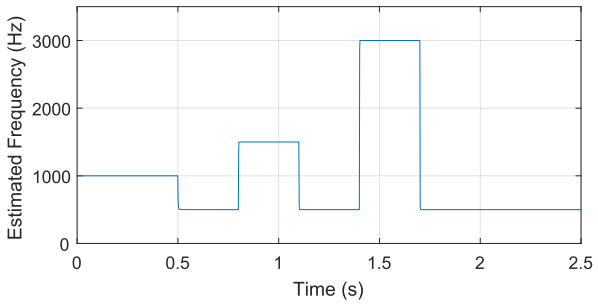

Fig. 11. Identified frequencies using PAA.

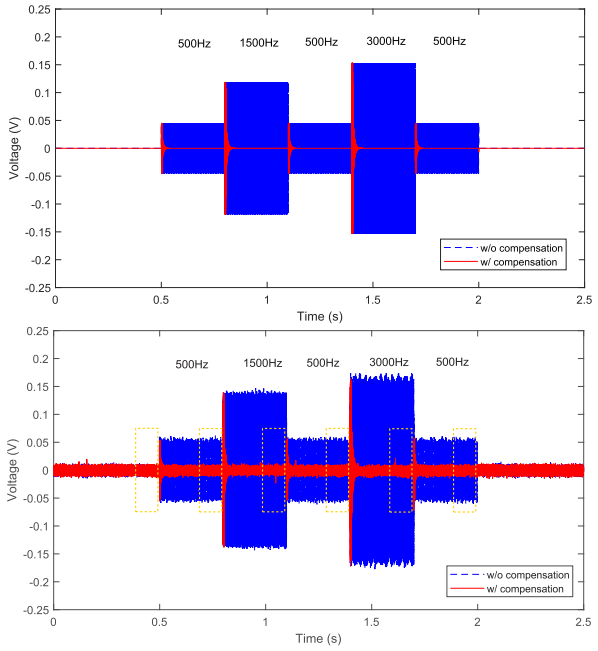

Fig. 12. Simulation (top) and experimental (bottom) results of rejecting narrowband disturbance with single step changing frequency.

TABLE I
2-NORM OF BASELINE NOISE AND RESIDUAL ERRORS

Period (s)	0.39→0.49 (Baseline)	0.69→0.79 (500Hz)	0.99→1.09 (1500Hz)
$\|e_r\|_2^2$ ($\times 10^{-1}$V^2)	1.652	1.451	1.373
Period (s)	1.29→1.39 (500Hz)	1.59→1.69 (3000Hz)	1.89→1.99 (500Hz)
$\|e_r\|_2^2$ ($\times 10^{-1}$V^2)	1.485	1.521	1.458

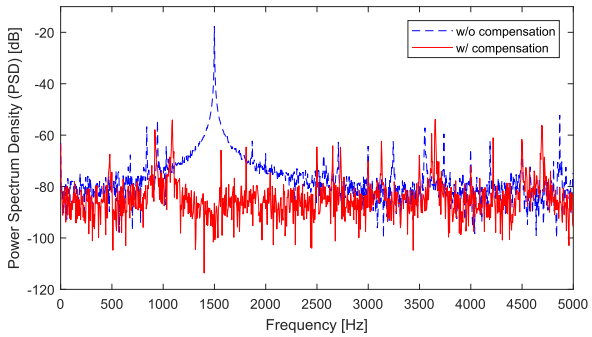

Fig. 13. Experimental results of error spectra of rejecting a 1500-Hz vibration.

periods. For large-range motions, major galvoscanner vendors provide image field correction algorithms that can eliminate nonlinear scanning errors.

The steady-state error spectra further reveal the effectiveness of the proposed scheme. Fig. 13 shows that when the system is subjected to a 1500-Hz vibration, the proposed scheme reduces the spectral peak from around -18 to -101 dB, indicating an attenuation of about 83 dB. This is directly reflected by the red dashed line in Fig. 14(a). The sensitivity function with the proposed scheme exhibits a deep notch at 1500 Hz and, at the same time, almost no amplification at other frequencies compared to the baseline case.

Despite that the galvoscanner system has highly accurate plant dynamics, to reveal the robustness of the proposed method, we perturbed the plant dynamics $P(z)$ by an uncertainty $\Delta(z)$ that is bounded by $\|1/T(z)\|_\infty$ [see Fig. 14(c)]. The weight of the uncertainty is filtered by a high-pass filter so that it is more significant at high frequencies and reaches maximum $[\|1/T(z)\|_\infty]$ near the Nyquist frequency. Fig. 14(d) shows the Nyquist plot of $L(z) = \tilde{P}(z)C_{\text{eq}}(z)$, where $\tilde{P}(z)$ is the perturbed plant and $C_{\text{eq}}(z)$ is the equivalent feedback controller of the proposed scheme given by (1). Clearly, the perturbed plots remain far away from the point $(-1, 0)$ and the original encirclement is not violated. In other words, the system remains robustly stable under the large perturbations. Fig. 14(a) and (b) shows the impact of uncertainty on feedback performance. The magnitude response of the sensitivity function fluctuates slightly at regions of high uncertainties; however, the designed notch at 1500 Hz is largely preserved and the algorithm still successfully rejects the narrowband disturbance. Note that if the plant uncertainty is large enough to violate (20), the closed-loop stability and

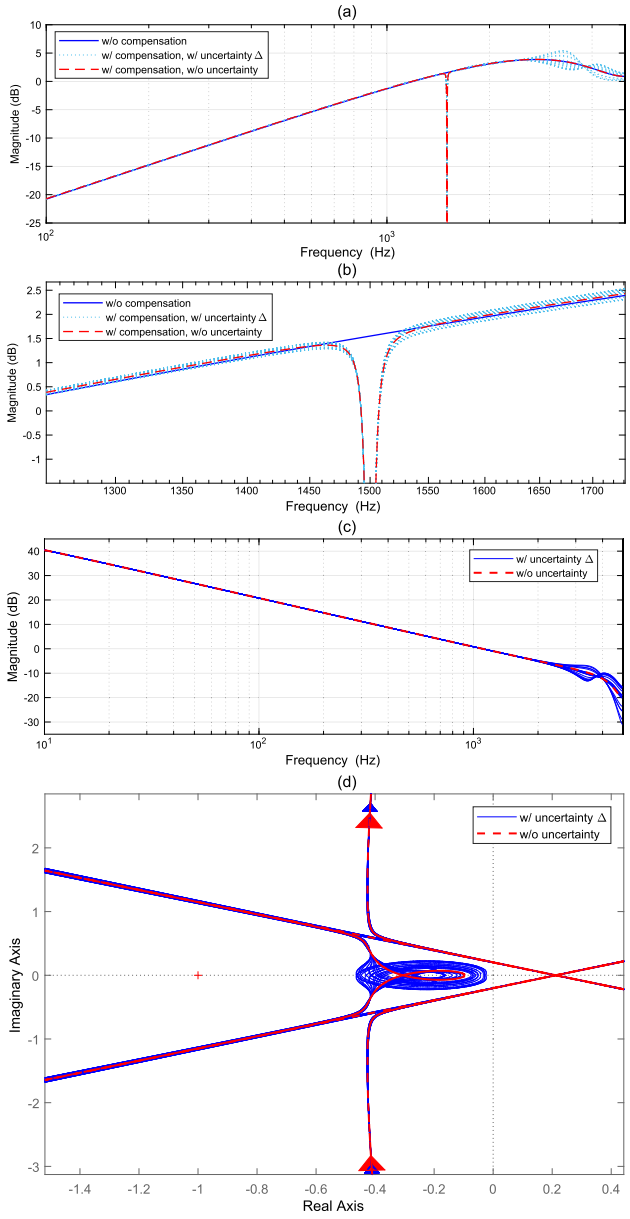

Fig. 14. Sensitivity functions' comparison and robust stability analysis. (a) Magnitude responses of the sensitivity functions under different conditions. (b) Zoomed-in view of sensitivity function around disturbance frequency. (c) Perturbed plant dynamics. (d) Nyquist plot of $L(z) = \tilde{P}(z)C_{\text{eq}}(z)$.

disturbance rejection performance cannot be guaranteed and high-performance control intrinsically has to be traded off to robust stability.

Two more simulation tests are conducted with increased disturbance complexity. The disturbances now contain, respectively, two and three frequency components in each period. The corresponding time series of the residual errors is shown in Fig. 15. Again, one can observe that the proposed scheme achieves the desired disturbance rejection rapidly.

The aforementioned regulation performance transforms analogously to tracking control with a nonzero reference. For laser scanning in additive manufacturing, Fig. 16 shows the rejection of two narrowband frequencies when r in Fig. 2 (red solid line in Fig. 16) is a periodic infill pattern

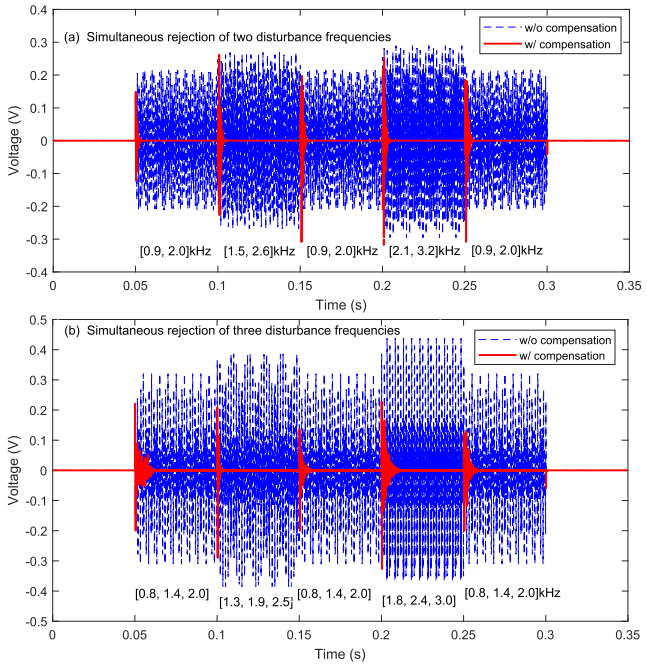

Fig. 15. Simulation results of rejecting narrowband disturbances with (a) two- and (b) three-step changing frequencies.

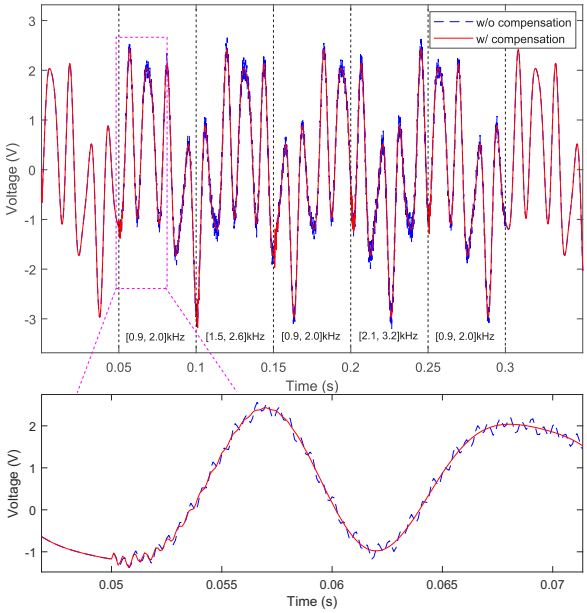

Fig. 16. Simulation results of rejecting narrowband disturbances with two-step changing frequencies with nonzero input.

(e.g., the WEAVE scanning [35]). It can be seen that the disturbances are rapidly rejected similar to the regulation performance.

Fig. 17 compares the proposed algorithm with a conventional DOB [21] and presents the results of rejecting the disturbance series described in Fig. 15(a). In the conventional DOB, a realizable nominal plant inverse model is used to filter the disturbance and a lattice-structure IIR filter is used to select the disturbance rejection region. The 3-dB bandwidth of the

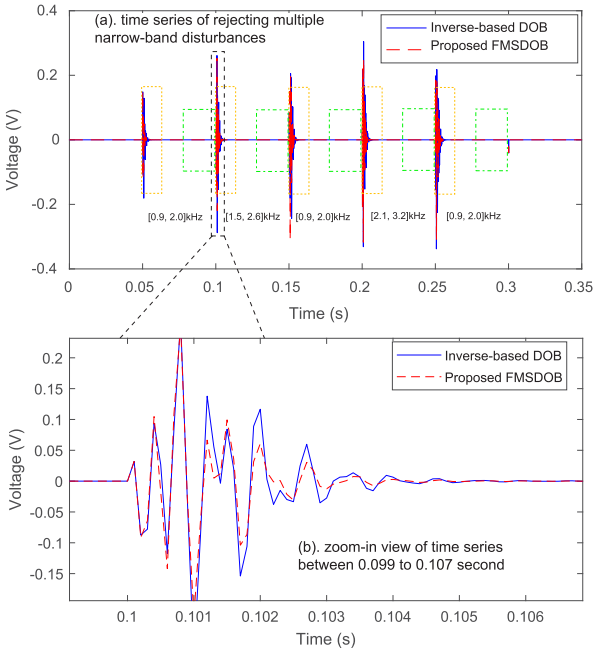

Fig. 17. Comparison of FMSDOB and inverse-based DOB on rejecting disturbance with multiple narrowband frequencies. (a) Time series of rejecting multiple narrowband frequencies. (b) Zoomed-in view of time series between 0.099 and 0.107 s.

TABLE II
RESULTS OF DISTURBANCE REJECTION WITH FMSDOB AND INVERSE-BASED DOB

Algorithm	**freq.** (kHz)	$\|e_t\|_2^2$ ($\times 10^{-1}$V^2)	max$\|e_r\|$ ($\times 10^{-5}$V)
FMSDOB	null$\rightarrow[0.9, 2.0]$	0.788	0.748
	$[0.9, 2.0]\rightarrow[1.5, 2.6]$	3.083	1.478
	$[1.5, 2.6]\rightarrow[0.9, 2.0]$	4.477	1.596
	$[0.9, 2.0]\rightarrow[2.1, 3.2]$	3.663	1.215
	$[2.1, 3.2]\rightarrow[0.9, 2.0]$	3.454	1.845
Inverse DOB	null$\rightarrow[0.9, 2.0]$	2.280	1.348
	$[0.9, 2.0]\rightarrow[1.5, 2.6]$	4.338	2.817
	$[1.5, 2.6]\rightarrow[0.9, 2.0]$	5.380	3.012
	$[0.9, 2.0]\rightarrow[2.1, 3.2]$	5.049	2.594
	$[2.1, 3.2]\rightarrow[0.9, 2.0]$	5.696	3.405

bandpass filters used in these two methods is set to be the same. It is seen that both methods achieve zero steady-state error. However, a zoomed-in view of Fig. 17 (bottom) shows that the average transient magnitude of the proposed scheme is lower than that of inverse-based DOB. This is further evaluated by computing two quantitative values: the 2-norm values of the transient errors (denoted as $\|e_t\|_2^2$) within the initial 15 ms after injection of compensation signal (indicated by yellow dashed frames in Fig. 17) and the maximum values of residual errors (denoted as $|e_r|$, the corresponding time windows are marked by green dashed frames in Fig. 17). The results are presented in Table II. The proposed algorithm yields better performance than the conventional DOB in both transient and steady-state responses, largely due to the inversion of the plant dynamics at only the needed locations.

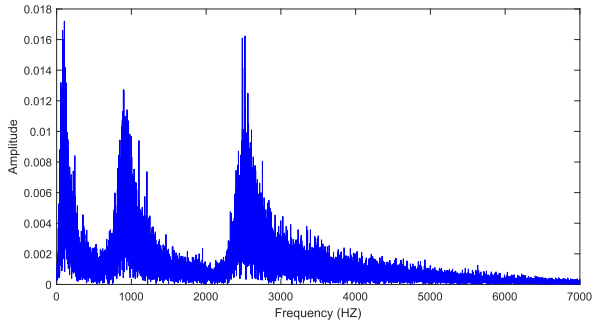

Fig. 18. Wideband disturbance in simulation.

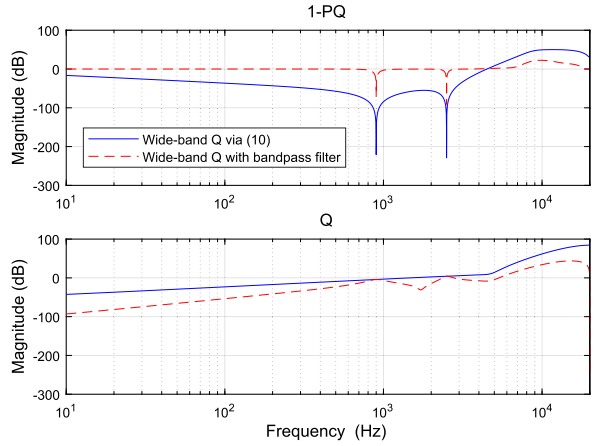

Fig. 19. Magnitude response of the 1-PQ and Q with wideband filter design.

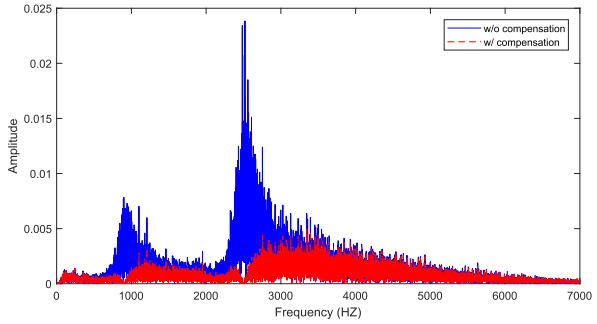

Fig. 20. Spectrum comparison with and without the proposed wideband Q compensator.

B. Wideband Disturbance

We now increase the sampling frequency of the system to obtain

$$\hat{P}(z) = \frac{0.0282z^2 + 0.1504z + 0.1146}{z^4 - 1.3190z^3 + 0.929z^2 - 0.6073z - 0.0035}$$

with $T_s = 2.5 \times 10^{-5}$ s. Note that this is a nonminimum-phase system with an unstable zero at $z = -4.419$.

To illustrate the performance of rejecting wideband vibrations, we feed a mockup disturbance signal (see Fig. 18) as $d(k)$ in Fig. 2. The disturbance mockup is a scaled version of actual acoustic vibrations in high-precision motion systems (Fig. 4) with three wide peaks centered around

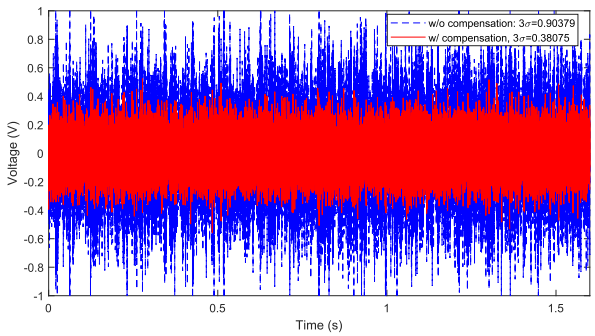

Fig. 21. Performance of the wideband Q-filter in the time domain.

100, 900, and 2500 Hz. The baseline sensitivity function is capable to attenuate low-frequency disturbances. Thus, in the Q-filter design, we only focus on the two faster disturbances (900 and 2500 Hz). Fig. 19 shows the frequency responses of the Q-filter and $1 - PQ$. As expected, two wide attenuation notches are located at the target frequencies in Fig. 19. The red dashed line shows the result of applying lattice bandpass filters for mitigating the waterbed effect at high frequencies. The frequency-domain disturbance rejection result is shown in Fig. 20. We can see that both the open- and closed-loop systems reject the energy peak at 100 Hz thanks to the baseline sensitivity function; as the disturbance frequency increases, the baseline control becomes ineffective. On the other hand, the proposed scheme is able to effectively attenuate the large spectral peaks. The time series in Fig. 21 further show the significant performance of the proposed scheme, with a 3σ value of the residual position error as low as 0.38 compared with 0.90 in the baseline system (a 57% reduction).

IX. Conclusion

In this article, an inverse-free FMSDOB is introduced for disturbance rejection in nonminimum-phase systems. By designing an FIR filter that selectively inverts the plant dynamics locally at the needed frequency regions, the proposed scheme avoids explicit inverse plant models in conventional high-performance disturbance compensation schemes and is hence particularly useful for plants containing unstable zeros or when a stable plant inversion is prohibitively expensive over the full frequency range. We provide both narrowband and wideband filter designs to, respectively, reject disturbance concentrating at individual frequencies and spanning over wide bands. Also discussed are methods for controlling the fundamental waterbed limitation. Under different complexity levels, simulation and experimentation on a galvo scanner platform in SLS additive manufacturing show significant performance gain for disturbance attenuation.

References

[1] X. Chen and M. Tomizuka, "A minimum parameter adaptive approach for rejecting multiple narrow-band disturbances with application to hard disk drives," *IEEE Trans. Control Syst. Technol.*, vol. 20, no. 2, pp. 408–415, Mar. 2012.

[2] L. Sun, T. Jiang, and X. Chen, "Adaptive loop shaping for wideband disturbances attenuation in precision information storage systems," *IEEE Trans. Magn.*, vol. 53, no. 5, May 2017, Art. no. 3301813.

[3] R. Ehrlich, J. Adler, and H. Hindi, "Rejecting oscillatory, non-synchronous mechanical disturbances in hard disk drives," *IEEE Trans. Magn.*, vol. 37, no. 2, pp. 646–650, Mar. 2001.

[4] J. Zeng and R. de Callafon, "Recursive filter estimation for feedforward noise cancellation with acoustic coupling," *J. Sound Vib.*, vol. 291, nos. 3–5, pp. 1061–1079, Apr. 2006.

[5] T. Jiang, H. Xiao, and X. Chen, "An inverse-free disturbance observer for adaptive narrow-band disturbance rejection with application to selective laser sintering," in *Proc. ASME Dyn. Syst. Control Conf.*, Tysons, VA, USA, vol. 3, Oct. 2017, Art. no. V003T32A006.

[6] J. Zheng, G. Guo, Y. Wang, and W. E. Wong, "Optimal narrow-band disturbance filter for PZT-actuated head positioning control on a spinstand," *IEEE Trans. Magn.*, vol. 42, no. 11, pp. 3745–3751, Nov. 2006.

[7] T. Atsumi, A. Okuyama, and M. Kobayashi, "Track-following control using resonant filter in hard disk drives," *IEEE/ASME Trans. Mechatronics*, vol. 12, no. 4, pp. 472–479, Aug. 2007.

[8] M. Steinbuch, "Repetitive control for systems with uncertain period-time," *Automatica*, vol. 38, no. 12, pp. 2103–2109, 2002.

[9] L. Cuiyan, Z. Dongchun, and Z. Xianyi, "A survey of repetitive control," in *Proc. IEEE/RSJ Int. Conf. Intell. Robots Syst.*, vol. 2, Sep./Oct. 2004, pp. 1160–1166.

[10] I. D. Landau, A. Constantinescu, and D. Rey, "Adaptive narrow band disturbance rejection applied to an active suspension—An internal model principle approach," *Automatica*, vol. 41, no. 4, pp. 563–574, Apr. 2005.

[11] I. D. Landau, M. Alma, J. J. Martinez, and G. Buche, "Adaptive suppression of multiple time-varying unknown vibrations using an inertial actuator," *IEEE Trans. Control Syst. Technol.*, vol. 19, no. 6, pp. 1327–1338, Nov. 2011.

[12] I. D. Landau, A. C. Silva, T.-B. Airimitoaie, G. Buche, and M. Noe, "Benchmark on adaptive regulation—Rejection of unknown/time-varying multiple narrow band disturbances," *Eur. J. Control*, vol. 19, no. 4, pp. 237–252, Jul. 2013.

[13] A. Karimi and Z. Emedi, "$\mathcal{H}_\infty$ gain-scheduled controller design for rejection of time-varying narrow-band disturbances applied to a benchmark problem," *Eur. J. Control*, vol. 19, no. 4, pp. 279–288, 2013.

[14] Q. Zheng and M. Tomizuka, "A disturbance observer approach to detecting and rejecting narrow-band disturbances in hard disk drives," in *Proc. 10th IEEE Int. Workshop Adv. Motion Control*, Mar. 2008, pp. 254–259.

[15] X. Chen and M. Tomizuka, "Overview and new results in disturbance observer based adaptive vibration rejection with application to advanced manufacturing," *Int. J. Adapt. Control Signal Process.*, vol. 29, no. 11, pp. 1459–1474, Nov. 2015.

[16] H. W. Bode, *Network Analysis Feedback Amplifier Design*. New York, NY, USA: Van Nostrand, 1945.

[17] G. Stein, "Respect the unstable," *IEEE Control Syst.*, vol. 23, no. 4, pp. 12–25, Aug. 2003.

[18] J. C. Doyle, B. A. Francis, and A. R. Tannenbaum, *Feedback Control Theory*. North Chelmsford, MA, USA: Courier Corporation, 2013.

[19] X. Chen, T. Jiang, and M. Tomizuka, "Pseudo Youla–Kucera parameterization with control of the waterbed effect for local loop shaping," *Automatica*, vol. 62, pp. 177–183, Dec. 2015.

[20] X. Chen and M. Tomizuka, "Optimal decoupled disturbance observers for dual-input single-output systems," *ASME J. Dyn. Syst., Meas., Control*, vol. 136, no. 5, 2014, Art. no. 051018.

[21] X. Chen and M. Tomizuka, "Selective model inversion and adaptive disturbance observer for time-varying vibration rejection on an active-suspension benchmark," *Eur. J. Control*, vol. 19, no. 4, pp. 300–312, Jul. 2013.

[22] A. C. Silva, I. D. Landau, L. Dugard, and X. Chen, "Modified direct adaptive regulation scheme applied to a benchmark problem," *Eur. J. Control*, vol. 28, pp. 69–78, Mar. 2016.

[23] X. Chen and M. Tomizuka, "Discrete-time reduced-complexity Youla parameterization for dual-input single-output systems," *IEEE Trans. Control Syst. Technol.*, vol. 24, no. 1, pp. 302–309, Jan. 2016.

[24] F. Ben Amara, P. T. Kabamba, and A. G. Ulsoy, "Adaptive sinusoidal disturbance rejection in linear discrete-time systems—Part I: Theory," *ASME J. Dyn. Syst., Meas., Control*, vol. 121, no. 4, pp. 648–654, Dec. 1999.

[25] F. Ben Amara, P. T. Kabamba, and A. G. Ulsoy, "Adaptive sinusoidal disturbance rejection in linear discrete-time systems—Part II: Experiments," *ASME J. Dyn. Syst., Meas., Control*, vol. 121, no. 4, pp. 655–659, 1999.

[26] R. de Callafon and C. E. Kinney, "Robust estimation and adaptive controller tuning for variance minimization in servo systems," *J. Adv. Mech. Des., Syst., Manuf.*, vol. 4, no. 1, pp. 130–142, 2010.

[27] B. Haack and M. Tomizuka, "The effect of adding zeroes to feedforward controllers," *ASME Trans. J. Dyn. Syst., Meas., Control*, vol. 113, no. 1, pp. 6–10, Mar. 1991.

[28] M. Tomizuka, "Zero phase error tracking algorithm for digital control," *ASME Trans. J. Dyn. Syst., Meas., Control*, vol. 109, no. 1, pp. 65–68, Mar. 1987.

[29] J. A. Butterworth, L. Y. Pao, and D. Y. Abramovitch, "Analysis and comparison of three discrete-time feedforward model-inverse control techniques for nonminimum-phase systems," *Mechatronics*, vol. 22, no. 5, pp. 577–587, 2012.

[30] K.-S. Kim and Q. Zou, "A modeling-free inversion-based iterative feedforward control for precision output tracking of linear time-invariant systems," *IEEE/ASME Trans. Mechatronics*, vol. 18, no. 6, pp. 1767–1777, Dec. 2013.

[31] J. S. Dewey, K. Leang, and S. Devasia, "Experimental and theoretical results in output-trajectory redesign for flexible structures," *J. Dyn. Syst., Meas., Control*, vol. 120, no. 4, pp. 456–461, 1998.

[32] D. S. Bernstein, *Matrix Mathematics: Theory, Facts, and Formulas with Application to Linear Systems Theory*. Princeton, NJ, USA: Princeton Univ. Press, 2005.

[33] K. S. Ramani, M. Duan, C. E. Okwudire, and A. G. Ulsoy, "Tracking control of linear time-invariant nonminimum phase systems using filtered basis functions," *J. Dyn. Syst., Meas., Control*, vol. 139, no. 1, pp. 011001-1–011001-11, Jan. 2017.

[34] J. V. Zundert and T. Oomen, "On inversion-based approaches for feedforward and ILC," *IFAC Mechatronics*, vol. 50, pp. 282–291, Apr. 2018.

[35] I. Gibson, D. Rosen, and B. Stucker, *Additive Manufacturing Technologies: 3D Printing, Rapid Prototyping, and Direct Digital Manufacturing*, 2nd ed. Springer-Verlag New York, 2015.

[36] *Installation Operation RTC5 Board for Real Time Control Scan Heads Laser*, Rev. 1.10e edition, SCANLAB AG, Munich, Germany, Oct. 2015.

[37] B. D. O. Anderson, "From Youla–Kucera to identification, adaptive and nonlinear control," *Automatica*, vol. 34, no. 12, pp. 1485–1506, 1998.

[38] C. E. Garcia and M. Morari, "Internal model control. A unifying review and some new results," *Ind. Eng. Chem. Process Des. Develop.*, vol. 21, no. 2, pp. 308–323, 1982.

[39] M. Shamsuzzoha and M. Lee, "IMC-PID controller design for improved disturbance rejection of time-delayed processes," *Ind. Eng. Chem. Res.*, vol. 46, no. 7, pp. 2077–2091, 2007.

[40] S. Aranovskiy and L. B. Freidovich, "Adaptive compensation of disturbances formed as sums of sinusoidal signals with application to an active vibration control benchmark," *Eur. J. Control*, vol. 19, no. 4, pp. 253–265, Jul. 2013.

[41] D. C. Youla, J. J. Bongiorno, and H. Jabr, "Modern Wiener–Hopf design of optimal controllers Part I: The single-input-output case," *IEEE Trans. Autom. Control*, vol. AC-21, no. 1, pp. 3–13, Feb. 1976.

[42] V. Kučera, "Stability of discrete linear feedback systems," *IFAC Proc. Volumes*, vol. 8, pp. 573–578, Aug. 1975.

[43] R. L. Burden and J. D. Faires, *Numerical Analysis*, 8th ed. Boston, MA, USA: Cengage Learning, 2004.

[44] K. Hirano, S. Nishimura, and S. Mitra, "Design of digital notch filters," *IEEE Trans. Circuits Syst.*, vol. CAS-21, no. 4, pp. 540–546, Jul. 1974.

[45] X. Chen and H. Xiao, "Multirate forward-model disturbance observer for feedback regulation beyond Nyquist frequency," *Syst. Control Lett.*, vol. 94, pp. 181–188, Aug. 2016.

Tianyu Jiang received the B.S. degree from the University of Science and Technology of China, Hefei, China, in 2014. He is currently pursuing the Ph.D. degree with the Department of Mechanical Engineering, University of Washington, Seattle, WA, USA.

His current research interests include theory and practice of dynamic systems and controls with application to additive and advanced manufacturing.

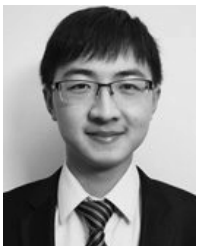

Hui Xiao was born in Yunnan, China. He received the B.S. degree from the Department of Mechanical Engineering, Tsinghua University, Beijing, China, in 2015. He is currently pursuing the Ph.D. degree with the Department of Mechanical Engineering, University of Washington, Seattle, WA, USA.

He was a Teaching Assistant and also a Research Assistant with the Department of Mechanical Engineering. His research interests include vision-based robot control.

Jiong Tang (M'09) received the B.S. and M.S. degrees in applied mechanics from Fudan University, China, in 1989 and 1992, respectively, and the Ph.D. degree in mechanical engineering from Pennsylvania State University, State College, PA, USA, in 2001.

He was a Mechanical Engineer with the GE Global Research Center, NY, USA, from 2001 to 2002. He then joined the Mechanical Engineering Department, University of Connecticut, Storrs, CT, USA, where he is currently a Professor and the Director of Dynamics, Sensing, and Controls Laboratory. His current research interests include structural dynamics and system dynamics, control, and sensing and monitoring.

Dr. Tang is a fellow of ASME. He currently serves as an Associate Editor for the IEEE/ASME TRANSACTIONS ON MECHATRONICS and served as an Associate Editor for the IEEE TRANSACTIONS ON INSTRUMENTATION AND MEASUREMENT from 2009 to 2012. He also served as an Associate Editor for the *ASME Journal of Vibration and Acoustics* and the *ASME Journal of Dynamic Systems, Measurement, and Control*.

Liting Sun received the B.S. degree in mechanical engineering from the University of Science and Technology of China, Hefei, China, in 2009. She is currently pursuing the Ph.D. degree with the Department of Mechanical Engineering, University of California, Berkeley, CA, USA.

She was a Visiting Researcher and Junior Specialist with the University of California at Berkeley, from 2012 to 2015. Her current research interests include intelligent and high-precision behavior design of autonomous systems based on learning and control, such as iterative learning control, adaptive precision motion control, and behavior and motion planning for mobile robots.

Xu Chen received the bachelor's degree (Hons.) from Tsinghua University, China, in 2008, and the M.S. and Ph.D. degrees in mechanical engineering from the University of California, Berkeley, CA, USA, in 2010 and 2013, respectively.

He is currently an Assistant Professor with the Department of Mechanical Engineering, University of Washington, Seattle, WA, USA. His current research interests include dynamic systems and controls, information fusion, advanced manufacturing, and intelligent machines.

Dr. Chen is a recipient of the U.S. National Science Foundation CAREER Award and the Young Investigator Award from the ISCIE/ASME International Symposium on Flexible Automation.